Retrieval of atmospheric $H^{15}NO_3/H^{14}NO_3$ isotope ratio profile from MIPAS/ENVISAT limb-scanning measurements

G. Brizzi,[1] E. Arnone,[2] M. Carlotti,[2] B. M. Dinelli,[3] J.-M. Flaud,[4] E. Papandrea,[2] A. Perrin,[4] and M. Ridolfi[2]

Received 21 November 2008; revised 13 May 2009; accepted 21 May 2009; published 25 August 2009.

[1] We report the first measurement of the isotopic partitioning between stratospheric $H^{14}NO_3$ and $H^{15}NO_3$. The vertical distribution of the isotope ratio of the two isotopologues of nitric acid was derived using the ν_5 band Q branch of $H^{15}NO_3$ that was recently identified in measurements from the MIPAS experiment using newly generated spectral line parameters for the minor isotopologue. Because of the very low intensity of the spectral features adopted for the retrieval, we established an "ad hoc" inversion procedure based on a regularized linear Kalman filter approach. This procedure permits the retrieval of the deviations from the natural $H^{15}NO_3/H^{14}NO_3$ isotope ratio profile, averaged over different latitude bands and time intervals, in the altitude range from 18 to 42 km. The resulting profiles show an overall substantial depletion with height of $H^{15}NO_3$, with respect to the natural partitioning, and no significant latitude and time dependence. The developed retrieval procedure can be readily extended to other atmospheric trace gas isotope ratios.

Citation: Brizzi, G., E. Arnone, M. Carlotti, B. M. Dinelli, J.-M. Flaud, E. Papandrea, A. Perrin, and M. Ridolfi (2009), Retrieval of atmospheric $H^{15}NO_3/H^{14}NO_3$ isotope ratio profile from MIPAS/ENVISAT limb-scanning measurements, *J. Geophys. Res.*, *114*, D16301, doi:10.1029/2008JD011504.

1. Introduction

[2] Nitric acid (HNO_3) is an atmospheric trace gas playing a key role in the chemistry of stratospheric ozone. In the middle atmosphere it constitutes an important reservoir molecule for both odd nitrogen (NO_x) and odd hydrogen (HO_x) oxide species, directly linking the two reactive chemical families. Furthermore, in the wintertime polar vortex, HNO_3 participates in the formation of Type 1 Polar Stratospheric Cloud (PSC I) particles which, by triggering both heterogeneous chemistry and denitrification of the lower stratosphere, determine the ozone hole phenomenon [*World Meteorological Organization*, 2003].

[3] The acknowledged photochemistry suggests that HNO_3 is produced in the stratosphere by gas phase reaction between hydroxyl radical and nitrogen dioxide in the presence of a collision partner (M) that carries away the dissociation energy and conserves the momentum balance,

$$(R1) \qquad OH + NO_2 + M \rightarrow HNO_3 + M,$$

and by conversion of N_2O_5 in a heterogeneous chemistry process with aerosol [*Austin et al.*, 1986]. N_2O_5 is, in turn, produced by gas phase reactions in Polar night conditions. The HNO_3 sinks are photodissociation,

$$(R2) \qquad HNO_3 + h\nu \rightarrow OH + NO_2,$$

and the solidification during PSC formation that leads to removal through sedimentation (denitrification).

[4] For its atmospheric relevance, the nitric acid distribution has been extensively studied with observations collected both in the stratosphere and in the troposphere, from the ground [e.g., *Rinsland et al.*, 1991; *Meier et al.*, 2005], from balloons [e.g., *von Clarmann et al.*, 1993; *Oelhaf et al.*, 1994], aircrafts [e.g., *Toon et al.*, 1989; *Blom et al.*, 1995; *Fischer et al.*, 1997], and from space [e.g., *Russell et al.*, 1988; *Koike et al.*, 2000; *Griesfeller et al.*, 2006; *Mencaraglia et al.*, 2006].

[5] Different spectroscopic techniques, including mass spectrometry and infrared (IR) absorption or emission, have been used to obtain accurate and precise measurements of atmospheric HNO_3.

[6] In the mid-IR, HNO_3 exhibits a strong signature at 11.2 μm mainly due to the ν_5 and $2\nu_9$ bands. These bands are located in a rather transparent atmospheric window, practically free of interfering contributions, which has been frequently used to remotely sense this species. By sounding this region, past and present spaceborne infrared experiments, such as the Atmospheric Trace Molecule Spectroscopy (ATMOS) [*Gunson et al.*, 1996], the Michelson Interferometer

[1]Harvard-Smithsonian Center for Astrophysics, Cambridge, Massachusetts, USA.
[2]Dipartimento di Chimica Fisica e Inorganica, Università di Bologna, Bologna, Italy.
[3]Istituto di Scienze dell'Atmosfera e del Clima, CNR, Bologna, Italy.
[4]Laboratoire Interuniversitaire des Systèmes Atmosphériques, Université Paris 7, Université Paris 12, CNRS, Créteil, France.

0148-0227/09/2008JD011504

for Passive Atmospheric Sounding (MIPAS) [*Fischer et al.*, 2000], the Tropospheric Emission Spectrometer (TES) [*Beer et al.*, 2001], and the Atmospheric Chemistry Experiment (ACE) [*Bernath et al.*, 2005], included HNO_3 measurements within the scientific objectives of the mission.

[7] Infrared remote-sensing techniques have also the potential to provide accurate information about the isotopic composition of several atmospheric constituents, complementary to concentration measurements.

[8] Measurements of the geographical and altitude distribution of isotopic species provide valuable insights into the dynamical and chemical processes taking place in the atmosphere.

[9] So far, isotopic analyses have been used to distinguish between biogenic and anthropogenic sources, to investigate the composition of primordial atmospheres studying molecules trapped within ice cores, to identify preferential reaction pathways leading to noticeable improvements in the knowledge of trace gas global atmospheric budgets and biogeochemical Earth cycles.

[10] In spite of the broad interest in atmospheric active nitrogen species, to date the nitrogen isotopic composition of HNO_3 in the atmosphere has not been investigated; whereas studies have been reported on the isotopic fractionation in nitrous oxides (mainly N_2O) or ammonia, and the coupling between soil and marine environments with the overlying atmosphere [see, e.g., *Park et al.*, 2004; *Toyoda et al.*, 2004; *Kaiser et al.*, 2002, 2006; *Kaye*, 1987; *Griffith et al.*, 2000]. From these studies it is known that stratospheric N_2O is ^{15}N enriched relatively to tropospheric N_2O, most likely because of the preferential photolysis of isotopically light N_2O and to kinetic isotope effects.

[11] Since precise spectroscopic parameters of isotopically substituted atmospheric molecules are becoming available, further advances in the understanding of the mechanisms leading to atmospheric isotope fractionation are possible. $H^{15}NO_3$ is the second most abundant isotopologue of nitric acid with a relative abundance $\alpha = 3.64(7) \times 10^{-3}$ calculated from the isotopic abundances of ^1H, ^{15}N, and ^{16}O [*Lide*, 2000] (atmospheric N_2 is the reference standard for nitrogen isotopic abundance). However, to the best of our knowledge, the $^{15}N/^{14}N$ isotope ratio distribution has never been reported for HNO_3 in the Earth's atmosphere. The recent inclusion of $H^{15}NO_3$ spectral line parameters, relative to the fundamental ν_5 band [*Perrin and Mbiaké*, 2006], into the scientific version of the MIPAS dedicated spectroscopic database provided the possibility to identify, for the first time, the $H^{15}NO_3$ species in the Earth's atmosphere [*Brizzi et al.*, 2007]. This finding suggested the exploitation of MIPAS satellite observations to investigate the behavior of ^{15}N in atmospheric nitric acid. The goal of the present work is dual: (1) establish the feasibility of $^{15}N/^{14}N$ retrievals from MIPAS measurements and (2) provide a first $^{15}N/^{14}N$ global evaluation, thereby filling a gap in the understanding of nitrogen chemistry in the atmosphere.

[12] In section 2 we recall the basic concepts of the MIPAS experiment. The strategy designed for the $H^{15}NO_3/H^{14}NO_3$ isotope ratio retrievals is presented in section 3, while the operational choices used in our analysis are described in section 4. In section 5 we present and discuss results obtained for different time and space domains. Finally, we draw our conclusions in section 6.

2. MIPAS Experiment

[13] MIPAS is an Earth observation instrument, developed by the European Space Agency (ESA) and operating on board the Environmental Satellite (ENVISAT) that was launched on a nearly polar orbit on 1 March 2002. The MIPAS experiment is based on a high-resolution Fourier transform spectrometer and is designed to provide continuous information on a number of atmospheric species that are relevant to several interlinked issues over ozone chemistry and Global Change. MIPAS measures the emission of the atmosphere in a wide spectral interval in the mid-IR with the limb-scanning observation technique. Starting from July 2002 nearly continuous measurements were obtained for the first 2 years of satellite operation. Because of problems with the mirror drive of the interferometer, MIPAS suspended its measurements at the end of March 2004. Operations with reduced spectral resolution were resumed in January 2005, and the experiment is fully operational to date. This paper refers to the nominal observation mode measurements of the first 2 years of MIPAS activity. In the nominal mode (operated for 80% of the measuring time) MIPAS measured consecutive backward looking limb scans with the lines of sight lying approximately in the orbit plane. Each limb scan was made of 17 observation geometries with tangent altitudes ranging from 6 to 68 km with steps of 3 or 5 km. The spectral resolution of the instrument was set to its maximum value of 0.035 cm^{-1} Full Width at Half Maximum (FWHM), unapodized. MIPAS spectra are analyzed by the ESA's ground processor to provide pressure at the tangent points, vertical distribution of temperature, and Volume Mixing Ratio (VMR) of six atmospheric key species (H_2O, O_3, CH_4, N_2O, HNO_3, and NO_2). For an exhaustive discussion of the MIPAS experiment, the reader is referred to *Fischer et al.* [2008], and references therein. The good quality of MIPAS products is demonstrated in a dedicated set of validation papers; in particular, the validation of MIPAS HNO_3 VMR profiles is reported by *Wang et al.* [2007]. While the operational data processing [*Ridolfi et al.*, 2000; *Carli et al.*, 2004; *Raspollini et al.*, 2006] carried out by ESA covers only the above-mentioned six atmospheric species, nonoperational science-oriented retrieval codes have proven that MIPAS spectra can provide information on minor atmospheric constituents, as well as on the distribution of some of the main isotopologues of these gases [*Fischer et al.*, 2008]. So far, MIPAS represents one of the best suited instruments for stratospheric isotope research from space, and significant studies have recently reported the retrieval of stable isotope relative abundances from its measurements. In particular, investigations on singly substituted ozone isotopic variants were made by *Piccolo et al.* [2007], while HDO profile information was produced by *Payne et al.* [2004, 2007] and *Steinwagner et al.* [2007].

3. Retrieval Strategy

3.1. Retrieval Algorithm

[14] Because of its extremely low concentration in the stratosphere, $H^{15}NO_3$ exhibits a limb emission ν_5 Q branch

with very weak features near 871 cm^{-1}. Numerical simulations show that the peak intensity of this branch in MIPAS spectra is about 60% of the spectral noise. This poor signal-to-noise ratio prevents the retrieval of $H^{15}NO_3$ VMR profiles from individual limb scans if no external constraints are used. As an additional complication, the spectral features of $H^{14}NO_3$ and $H^{15}NO_3$ strongly overlap at the MIPAS spectral resolution, therefore the inversion algorithm must properly take into account the reciprocal interference of the two isotopologues.

[15] In order to derive information on the $H^{15}NO_3$ distribution from MIPAS spectra, we developed a dedicated inversion algorithm based on the Geofit Multi-Target Retrieval (GMTR) [*Carlotti et al.*, 2006]; only the Multi-Target capability of the GMTR algorithm but not its two-dimensional retrieval approach was exploited in this work (the 2-D representation is used for all atmospheric fields but the retrieved targets for which the horizontal homogeneity is assumed).

[16] The implemented algorithm retrieves simultaneously the profiles of both the $H^{14}NO_3$ VMR (hereinafter indicated as $\mathbf{x}$) and of the quantity $\mathbf{r}$ linked to the $H^{15}NO_3/H^{14}NO_3$ isotope ratio as follows: at each altitude z_i ($i = 1, \ldots, n$), the element r_i is defined as:

$$r_i = \frac{1}{\alpha} \cdot \frac{VMR_{H^{15}NO_3}(z_i)}{VMR_{H^{14}NO_3}(z_i)} \equiv \frac{1}{\alpha} \cdot \frac{VMR_{H^{15}NO_3}(z_i)}{x(z_i)} \quad (1)$$

where α is the relative standard abundance of $H^{15}NO_3$ ($\alpha = 3.64(7) \times 10^{-3}$). It is worth further emphasizing that the quantity $\mathbf{r}$ reports the deviations we observe from the natural $H^{15}NO_3/H^{14}NO_3$ isotope ratio profile.

[17] In the literature isotopic ratios are often reported using the so-called δ notation. Throughout this paper we report the results in terms of $\mathbf{r}$ because it is the direct output of our retrieval tools. The value of δ_i (δ at altitude z_i), expressed in units of per mil, can be easily obtained from r_i using:

$$\delta_i = 1000 \cdot (r_i - 1). \quad (2)$$

In our retrievals the two targets $\mathbf{x}$ and $\mathbf{r}$ are simultaneously determined with an iteratively Tikhonov-regularized optimal estimation approach [*Rodgers*, 2000; *Doicu et al.*, 2004] applied to the observations of individual limb scans. For convenience we define a column vector $\mathbf{z}$ that contains the components of both $\mathbf{x}$ and $\mathbf{r}$, i.e., $\mathbf{z} \equiv (x_1, x_2, \cdots, x_n, r_1, r_2, \cdots, r_n)^T$. Let h be the index numbering the individual limb scans to be processed. At each iteration, the retrieval operating on the observations $\mathbf{y}(h)$ with noise error covariance $\mathbf{S}_{y(h)}$ updates the current estimate $\mathbf{z}_0(h)$ according to:

$$\hat{\mathbf{z}}(h) \equiv \begin{pmatrix} \hat{\mathbf{x}}(h) \\ \hat{\mathbf{r}}(h) \end{pmatrix} = \mathbf{z}_0(h) + \left(\mathbf{K}^T\mathbf{S}_{y(h)}^{-1}\mathbf{K} + \mathbf{R}(h)\right)^{-1} \cdot \left(\mathbf{K}^T\mathbf{S}_{y(h)}^{-1}(\mathbf{y}(h) - \mathbf{F}(\mathbf{z}_0(h))) + \mathbf{R}(h)(\mathbf{z}_a(h) - \mathbf{z}_0(h))\right). \quad (3)$$

In this expression, where for simplicity we omit the iteration index, $\mathbf{F}(\mathbf{z}(h))$ is the forward model simulating the limb radiance for atmospheric state $\mathbf{z}(h)$, $\mathbf{K}$ is its Jacobian matrix calculated for $\mathbf{z} = \mathbf{z}_0(h)$, $\mathbf{z}_a(h)$ is an a priori estimate of $\mathbf{z}$ and $\mathbf{R}(h)$ is a constraint matrix that includes both the error covariance of $\mathbf{z}_a(h)$ and a Tikhonov regularization term. Considering that the state $\mathbf{z}$ includes both targets $\mathbf{x}$ and $\mathbf{r}$, $\mathbf{R}(h)$ can be written as

$$\mathbf{R}(h) = \begin{pmatrix} \mathbf{S}_{x_a}^{-1} & \mathbf{0} \\ \mathbf{0} & \mathbf{S}_{r_a}^{-1}(h) \end{pmatrix} + \begin{pmatrix} \gamma_x\mathbf{L}^T\mathbf{L} & \mathbf{0} \\ \mathbf{0} & \gamma_r(h)\mathbf{L}^T\mathbf{L} \end{pmatrix} \quad (4)$$

where $\mathbf{S}_{x_a}$ and $\mathbf{S}_{r_a}(h)$ are the error covariance matrices of the a priori estimates $\mathbf{x}_a$ and $\mathbf{r}_a(h)$, respectively, that constitute $\mathbf{z}_a(h) \equiv (\mathbf{x}_a^T, \mathbf{r}_a^T(h))^T$. $\mathbf{L}$ is the numerical first derivative operator while the scalars γ_x and $\gamma_r(h)$ are user supplied parameters driving the strength of the regularization. When convergence is reached, the error covariance matrix $\mathbf{S}_z(h)$ of the solution $\hat{\mathbf{z}}(h)$ provided by equation (3) is given by [*Rodgers*, 2000]:

$$\mathbf{S}_z(h) \equiv \begin{pmatrix} \mathbf{S}_x(h) & \mathbf{S}_{x,r}(h) \\ \mathbf{S}_{x,r}(h) & \mathbf{S}_r(h) \end{pmatrix} = \left(\mathbf{K}^T\mathbf{S}_{y(h)}^{-1}\mathbf{K} + \mathbf{R}(h)\right)^{-1}. \quad (5)$$

This matrix quantifies the mapping onto the solution of both the noise error of the measurements and the error associated with the a priori estimates $\mathbf{x}_a$ and $\mathbf{r}_a(h)$. The off diagonal elements of $\mathbf{S}_z(h)$ properly account for the covariances (and hence correlations) among the components of the state vector $\mathbf{z}$. In particular, covariances between individual profile components are estimated by the off diagonal elements of $\mathbf{S}_x(h)$ and $\mathbf{S}_r(h)$; while cross covariances between components of $\mathbf{x}$ and $\mathbf{r}$ are estimated by the elements of $\mathbf{S}_{x,r}(h)$ [*Dinelli et al.*, 2004].

[18] In order to reduce the noise error of $\mathbf{r}$, we apply the inversion approach outlined above, sequentially, to preselected sets of limb scans. While the target $\mathbf{x}$ can vary considerably from scan to scan, if we restrict the study to seasonal and gross latitudinal variability, $\mathbf{r}$ can be assumed constant within suitable time and latitude bins. Of course, the size of these bins determines the trade-off between the achieved noise error and the temporal and geographical resolution of the study. After selecting sets of limb scans (see section 4.2) for which we assume $\mathbf{r}$ constant, we sequentially apply the retrieval to the individual limb scans within each set. The constraints of the retrieval are set up as follows:

[19] 1. The first constraint is for profile $\mathbf{x}$. For $\mathbf{x}_a$ we use the profile retrieved with the GMTR algorithm from the same limb scan. This choice is motivated by the fact that the GMTR products are considered more accurate than the routine ESA Level 2 products [*Arnone and Carlotti*, 2008; *Arnone et al.*, 2009]. We build $\mathbf{S}_{x_a}$ by artificially associating to $\mathbf{x}_a$ a 100% error, uncorrelated. We apply only a weak Tikhonov regularization to $\mathbf{x}$ ($\gamma_x \approx 10$ $ppmv^{-2}$).

[20] 2. The second constraint is for profile $\mathbf{r}$. For the analysis of the first limb scan ($h = 1$) of each selected set we use $\mathbf{r}_a(1) = \mathbf{1}$ and we build $\mathbf{S}_{r_a}(h = 1)$ by assigning to $\mathbf{r}_a(1)$ a 100% error, uncorrelated. We select a weak Tikhonov regularization for $\mathbf{r}$ ($\gamma_r(h = 1) \approx 10$). For the subsequent analyzed limb scans ($h > 1$) we use $\mathbf{r}_a(h) = \hat{\mathbf{r}}(h - 1)$ and $\mathbf{S}_{r_a}(h) = \mathbf{S}_r(h - 1)$ (i.e., we use as a priori estimate the profile $\mathbf{r}$ obtained from the scans processed so far, with its full error covariance calculated from equation (5)). No further regularization is applied to $\mathbf{r}$ (i.e., $\gamma_r(h) = 0$ for $h > 1$).

[21] Note that as far as the target **r** is concerned, the retrieval approach used here is equivalent to a linear (the identity) Kalman filter [*Kalman*, 1960; *Rodgers*, 2000].

[22] The atmospheric fields: pressure, temperature, and VMR of the species other than HNO_3 (i.e., H_2O, O_3, CH_4, N_2O, and NO_2) are taken from the GMTR Level 2 products derived with the two-dimensional analysis of the corresponding limb scans (MIPAS-2D data, available on the dedicated Web site http://www.mbf.fci.unibo.it/mipas2d.html). For the remaining atmospheric constituents we assumed the profiles reported in the MIPAS dedicated climatological profile database [*Remedios et al.*, 2007].

[23] In order to better quantify the overall strength of the constraints applied to the retrieval process we exploit the averaging kernel (AK) matrix as a diagnostic tool. This matrix is used to characterize the vertical resolution of the retrieval and the degrees of freedom (DOF) of the inversion [*Rodgers*, 2000]. The element $\mathbf{A}_{k,m}(h)$ of the AK is defined as:

$$\mathbf{A}_{k,m}(h) = \frac{\partial \widehat{\mathbf{z}}_k(h)}{\partial \mathbf{z}_m}. \tag{6}$$

The calculation of the derivatives of the solution $\widehat{\mathbf{z}}(h)$ with respect to the components of $\mathbf{x}(h)$ is a relatively easy task because the real state $\mathbf{x}(h)$ is allowed to change from scan to scan. This implies that the only term depending on the true state $\mathbf{x}(h)$ on the right side of equation (3) is $\mathbf{y}(h)$. Therefore the part of the AK relating to the only target $\mathbf{x}(h)$ is given by:

$$\mathbf{A}_{\mathrm{x}}(h) \equiv \frac{\partial \widehat{\mathbf{x}}(h)}{\partial \mathbf{x}} = \left(\mathbf{K}^T \mathbf{S}_{\mathrm{y}(h)}^{-1} \mathbf{K} + \mathbf{R}(h)\right)^{-1} \cdot \mathbf{K}^T \mathbf{S}_{\mathrm{y}(h)}^{-1} \mathbf{K}. \tag{7}$$

The calculation of the derivatives with respect to **r** of equation (6) is more difficult because the true state **r** is assumed to be constant within the selected set of limb scans sequentially processed. Therefore, according to the applied constraints (see point 2 above), in (3) also $\mathbf{R}(h)$ (through $\mathbf{S}_{\mathrm{r_a}}(h)$) and $\mathbf{r}_{\mathrm{a}}(h)$ depend on the true state **r**. These derivatives can be calculated analytically using a few simplifying hypotheses:

[24] 1. If we assume linearity, we consider the solution $\widehat{\mathbf{z}}(h)$ as obtained from a single iteration of equation (3), with $\mathbf{z}_0(h)$ independent from the scan h.

[25] 2. If we assume uncorrelated targets **x** and **r** within each processed limb scan, this is justified because within each individual inversion in equation (3) the part related to **r** of matrix $\mathbf{K}^T\mathbf{S}_{\mathrm{y}(h)}^{-1}\mathbf{K} + \mathbf{R}(h)$ is always dominated by the term $\mathbf{R}(h)$ in which, according to equation (4), the correlations between **x** and **r** do not appear.

[26] 3. If we assume that the error covariance $\mathbf{S}_{\mathrm{y}(h)}$ does not depend on the considered limb scan h ($\mathbf{S}_{\mathrm{y}(h)} \equiv \mathbf{S}_{\mathrm{y}}$), this is justified because the instrument performance is expected to be mostly constant within large time intervals (a few weeks).

[27] With these assumptions, we can make explicit the dependence of $\mathbf{R}(h)$ and of $\mathbf{r}_{\mathrm{a}}(h)$ on the observations $\mathbf{y}(m)$ with $m = 1, \ldots, h$ in equation (3). After a few algebraic manipulations the part of the AK related to **r** is:

$$\mathbf{A}_{\mathrm{r}}(h) \equiv \frac{\partial \widehat{\mathbf{r}}(h)}{\partial \mathbf{r}} = \left(h\mathbf{K}_{\mathrm{r}}^T \mathbf{S}_{\mathrm{y}}^{-1} \mathbf{K}_{\mathrm{r}} + \mathbf{R}_{\mathrm{r}}(h=1)\right)^{-1} \cdot h\mathbf{K}_{\mathrm{r}}^T \mathbf{S}_{\mathrm{y}}^{-1} \mathbf{K}_{\mathrm{r}} \tag{8}$$

where the subscript "r" denotes matrices limited to the part referring to the elements of the target **r**. Note that as expected, if $\mathbf{K}_{\mathrm{r}}^T\mathbf{S}_{\mathrm{y}}^{-1}\mathbf{K}_{\mathrm{r}}$ is nonsingular, then $\mathbf{A}_{\mathrm{r}}(h)$ tends to the identity matrix for $h \to \infty$. At a first glance the assumptions made to derive this expression may seem relatively rough, however we checked the accuracy of expression (8) by comparison with direct numerical calculation of the derivatives (6) for a selected test case and found its accuracy to be a few percents. This accuracy is more than satisfactory considering that $\mathbf{A}_{\mathrm{r}}(h)$ is used here only as a diagnostic tool to quantify the deterioration of the vertical resolution of the retrieval due to the applied constraints.

[28] Compared to the simpler methods of averaging **r** profiles retrieved from individual limb scans, or retrieving a single **r** profile from an average spectrum, the retrieval approach used in this work offers the advantage of being more rigorous and accurate. Averaging of profiles retrieved by making heavy use of a priori information is problematic: profiles are not fully independent from each other because they are derived using the same a priori information. Retrieval of a single profile from an average spectrum implies the underlying assumption of linearity of the observed spectrum as a function of the retrieved quantities. Considering that the spectral features of $H^{15}NO_3$ addressed in this work overlap with strong $H^{14}NO_3$ features, the linearity assumption would be a crude approximation.

3.2. Self-Consistency of the Retrieval Algorithm

[29] Before the application to real data, we tested the self-consistency of the developed retrieval system on the basis of synthetic observations. We simulated several sets of MIPAS limb measurements corresponding to a full orbit (72 scans), assuming as a reference the ESA Level 2 HNO_3 profiles (**x**) and **r** = 1. In this self-consistency check we assumed as "real" the atmospheric HNO_3 distribution retrieved by the ESA Level 2 processor, while we started the retrieval using as initial guess the two-dimensional GMTR HNO_3 retrievals. We used this approach to make the test more realistic: we wanted to start from the same initial guess used in the retrievals from real data and, at the same time, we did not want to start the retrieval already from the "true" profiles. The sets of simulated observations differed only for the artificial noise added to the spectra. We tested cases with standard deviation equal to the actual MIPAS Noise Equivalent Spectral Radiance (NESR) and with standard deviation equal to NESR/10. In these test retrievals we used various initial guesses for **x** and **r**. In all tested cases we found good agreement between the retrieved targets and the reference profiles assumed for the generation of the synthetic observations. Figure 1 shows an example of results for the target **r**: in this test the standard deviation of the noise added to the synthetic observations was reduced by a factor 10 with respect to the MIPAS NESR, therefore the error bars, that represent the mapping of the measurement noise onto the retrieval, are much smaller than in the case of real observations. Figure 1 shows that the retrieval system is able to recover the reference atmospheric state with precision consistent with the amplitude of the adopted spectral noise. We conclude that possible artifacts introduced in the retrieved profiles by the inversion system have amplitude at least a

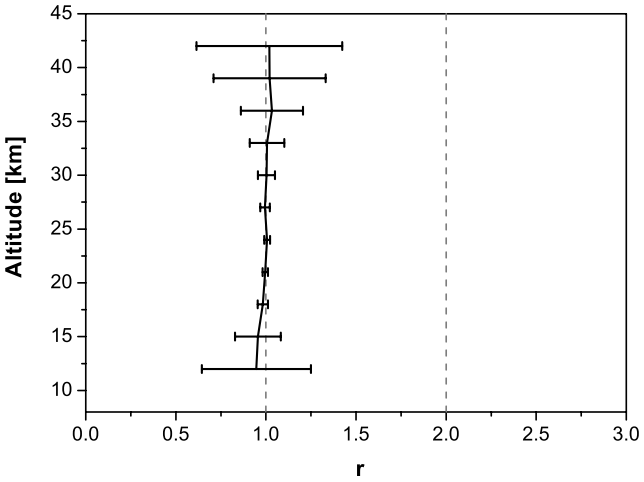

Figure 1. Result of a test retrieval with synthetic observations affected by a measurement noise with standard deviation equal to 1/10 of the MIPAS NESR. The inversion algorithm is able to recover within the error margins the profile $\mathbf{r}_{REF} = 1$ used in the synthetic observations. The dashed vertical line $\mathbf{r} = 2$ represents the initial guess profile assumed for the retrieval.

factor of 10 smaller than the error due to the real MIPAS noise.

4. Operational Choices

4.1. Spectral Intervals and Spectroscopic Data

[30] Our retrieval operates the simultaneous fitting of three different spectral intervals. The first two (876.375–879.375 cm^{-1} and 885.100–888.100 cm^{-1}) coincide with those used by the ESA Level 2 processor to routinely retrieve nitric acid VMR profiles [*Raspollini et al.*, 2006]. The third selected interval (870.000–871.500 cm^{-1}) contains the Q branch spectral features of the $H^{15}NO_3$ fundamental ν_5 band (see *Brizzi et al.* [2007, Figure 4] where the 870.000–871.500 cm^{-1} interval is reported together with simulations that highlight the contribution of the ^{15}N isotopologue). While the first two spectral intervals are selected using a dedicated algorithm [*Dudhia et al.*, 2002] aiming at the minimization of the total retrieval error, the third interval is rather a compulsory choice, given the paucity of the $H^{15}NO_3$ spectral features in the MIPAS bands. As pointed out by *Brizzi et al.* [2007], in the observed limb emission spectrum these features are embedded in much stronger features belonging to the $H^{14}NO_3$ isotopologue. For the simulation of the mentioned spectral intervals our forward model uses the MIPAS dedicated spectroscopic line database [*Flaud et al.*, 2003a, 2003b, 2006] complemented with $H^{15}NO_3$ line data as specified by *Brizzi et al.* [2007].

4.2. Error Budget Evaluation and Selection of Sets of Measurements

[31] With the implemented retrieval approach, the error of **r** due to measurement noise (the square roots of the diagonal elements of $\mathbf{S}_r$ from equation (5)) decreases as long as additional limb scans are included in the sequential analysis (see Figure 2). Of course the noise error reduction achieved depends on the altitude of the considered retrieval grid point. At the altitudes where the observations contain only little or no information on **r** the achieved reduction is negligible.

[32] The trade-off between the random error of **r** and the inaccuracy introduced by the assumption of time and geographical invariance of **r** drives the choice of the size of the sets of limb scans sequentially processed to derive a single **r** profile. The systematic error affecting **r** needs also to be considered for this choice. The random component should not exceed the systematic component in the error budget. On the other hand it is not wise to achieve a random error much smaller than the systematic one at the expenses of a much wider temporal/spatial resolution of the study. For this reason, prior to the selection of the sets of measurements to

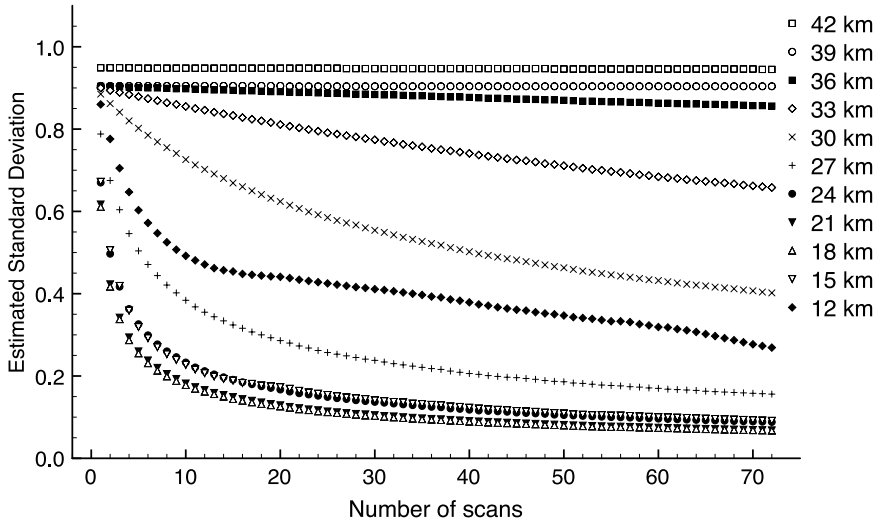

Figure 2. Reduction of the noise error achieved as long as limb scans, numbered in the horizontal axis, are included in the sequential analysis. As indicated in the plot key, different curves refer to different altitudes of the retrieval grid points.

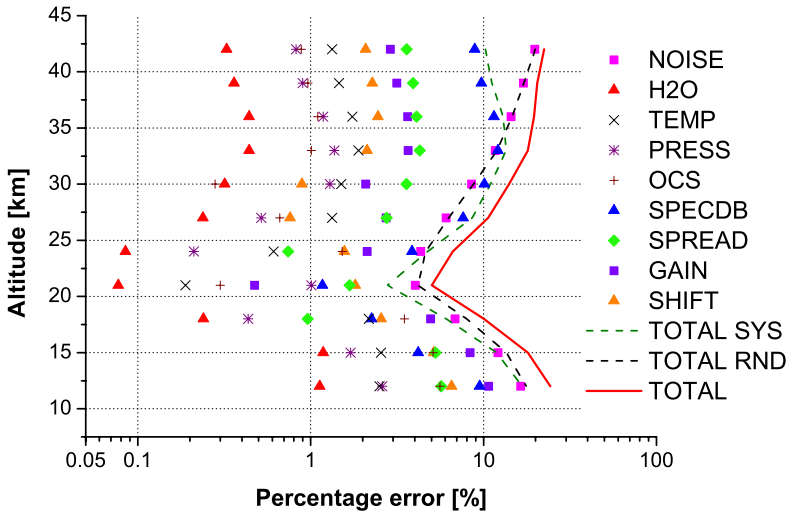

Figure 3. Total error budget and error components of the **r** profile assuming a sequential analysis of 400 MIPAS limb scans. See text for the description of the individual components.

be sequentially processed, we evaluated the error components, beside the measurement noise, that affect the targets of the retrieval using a standard perturbation analysis. This consisted of (1) generation of synthetic observations corresponding to experimental conditions in which a given parameter was perturbed/unperturbed with respect to a reference value and (2) calculation of the difference between target parameters retrieved with the sequential approach outlined in section 3.1 using perturbed and unperturbed observations.

[33] The error sources considered in our analysis include uncertainties in pressure (PRESS), temperature (TEMP), not retrieved and spectrally interfering species (H_2O and OCS turn out to be the main interfering gases), spectroscopic line database uncertainties (SPECDB), and errors on instrumental parameters such as the width of the instrument line shape (SPREAD), the spectral (SHIFT) and intensity (GAIN) calibrations [see *Fischer et al.*, 2008]. The perturbations applied to the atmospheric or model parameters listed above are consistent with those commonly adopted to evaluate the error budget of the MIPAS key products derived by the ESA Level 2 processor, as specified by A. Dudhia (http://www.atm.ox.ac.uk/group/mipas).

[34] Among the considered error sources, some of them are constant (i.e., SPECDB) or have a small variation (i.e., SPREAD, SHIFT, and GAIN) within the considered set of measurements, therefore producing a systematic bias in our results. Other error sources, such as PRESS, TEMP, and VMR of interfering species are considered to vary randomly from scan to scan, therefore their final contribution to the total error on **r** scales inversely proportional to the square root of the number of scans (n) included in the sequential analysis.

[35] Several values of n were tested. In Figure 3 we plot, as a function of altitude, the total error budget and the percentage contributions generated by each error source when it propagates through the sequential processing of 400 MIPAS limb scans. The component labeled as "NOISE" refers to the propagation of the measurement noise error into the solution of the inversion and, unlike the other components, is derived from the covariance matrix $\mathbf{S}_r$ of equation (5). Also reported is the total systematic error (TOTAL SYS) calculated by summing in quadrature the errors assumed constant in our sample (SPECDB, SHIFT, SPREAD, and GAIN). Similarly, we calculated the total random error (TOTAL RND) by summing in quadrature the errors that change randomly in our sample (NOISE, TEMP, PRESS, and VMR of interfering species). Finally, we calculated the total error (TOTAL) by summing in quadrature the TOTAL RND and TOTAL SYS errors.

[36] Figure 3 shows that n = 400 limb scans is a reasonable size for the set of measurements to include in a sequential analysis to derive a single **r** profile: under this condition the random error is of the same order of magnitude as the systematic one. We note also that given the MIPAS data acquisition rate, extending the size of the sequential analysis much beyond 400 limb scans would imply a significant limitation of the temporal and/or spatial resolution of the variability study, with a marginal further reduction of the random error. As shown in Figure 3, the total error of **r** tends to become large for altitudes outside the 12–42 km interval, therefore we limited the retrieval to this altitude range.

[37] The smoothing error is not included in the error budget because its evaluation requires the knowledge of the covariance matrix representing the atmospheric variability of the target profile under consideration (**r**) [*Rodgers*, 2000]. Such a covariance matrix is not available today, as no measurements of the **r** profile have been performed. Instead of providing the smoothing error we provide the AKs of the retrieval. The AKs will permit to calculate the smoothing error once a covariance matrix of the atmospheric variability of **r** will become available. The approach of providing AKs instead of the smoothing error is a very standard procedure (see, e.g., the validation papers given by *Hartogh and Espy* [2006–2009]).

4.3. Filtering of Measurements

[38] In order to guarantee that only good quality measurements contribute to the statistics accumulated in our sequential analysis, we applied a few quality checks both to the spectra to be processed and to the retrieved profiles.

[39] Since our forward model does not account for clouds in the field of view (FOV) of the instrument, we applied a

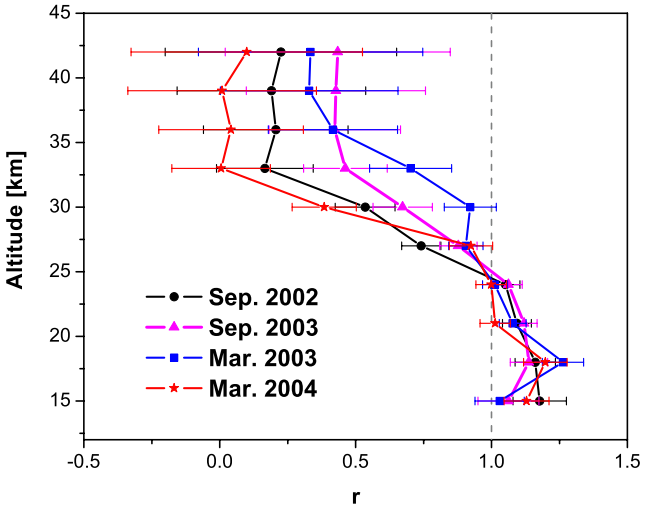

Figure 4. The **r** profiles retrieved from the midlatitude equinox (MID-e) sets of MIPAS measurements (entry for Figure 5c in Table 1). See text for details.

filter to exclude cloudy sweeps from our analysis. The cloud filter consists of the computation of a proxy, named Cloud Index (CI) [*Spang et al.*, 2004], for the presence of a cloud in the FOV. We considered a limb emission spectrum cloudy (and we excluded it from the analysis) if $CI < 6$. This threshold is usually considered very conservative [*Spang et al.*, 2004] for cloud detection, thus guaranteeing the clear sky data needed for the analysis.

[40] The results of the inversion of an individual limb scan are then fed in the sequential analysis only if both the following conditions are fulfilled:

[41] 1. The normalized L_2 weighted norm of the residuals (or chi-square, χ^2) is less than 2.5. This criterion excludes from the sequential analysis all the limb scans for which the final χ^2 of the inversion is an outlier of the statistical distribution of the χ^2.

[42] 2. The HNO_3 VMR at 12 km altitude is less than 0.002 ppmv (0.003 ppmv for the Polar regions). This criterion excludes limb scans providing unphysically high HNO_3 VMR values from the analysis.

5. Selection of Case Studies

[43] Aiming at the study of the $^{15}N/^{14}N$ isotope ratio profile under different latitudinal and seasonal conditions, subsets of MIPAS measurements (L1b data version 4.61) were selected around equinoxes and solstices, for the time period ranging from July 2002 to March 2004. Following the assumption made in section 3, the sequential retrieval was applied to sets of measurements collected in consecutive days within predefined latitude bands. **r** profiles were derived in four different latitude bands defined as: North Pole (NP) from 60°N to 90°N, South Pole (SP) from 60°S to 90°S, midlatitudes (MID) 60–20°S and 20–60°N, and equatorial (EQU) from 20°N to 20°S. A test performed on separated north and south midlatitude measurements showed that within the uncertainties of our analysis, there was no need to distinguish between them. The filtering process applied to MIPAS measurements (described in section 4.3) retained in the analysis equivalent sets of observations starting from 15 km tangent altitude. In the case of the EQU latitudinal band, the lower limit was set to 18 km. Table 1 provides details about the sets of observations considered in the selected case studies: the time intervals and the number of analyzed limb scans for each set of observations are reported in the third column of Table 1. As shown in Table 1, each of the considered case studies includes four sets of MIPAS measurements with a comparable number of limb scans. The first step of the study was to establish whether the four sets of data provide results that are consistent among themselves. Within each case study, the individual profiles are in good agreement within 2σ error. As a representative example, Figure 4 shows the four profiles relative to case MID-e of Table 1. This consistency supports the assumption of negligible variability of the **r** profile within the sets of limb measurements included in the sequential analysis. Given the reciprocal consistency of the retrieved **r** profiles, for each latitude band the best estimate of **r** can be calculated as the weighted average of the estimates derived from the four sets of measurements.

6. Results

[44] Figure 5 shows the mean profiles as determined from MIPAS observations for the selected latitude bands at equinoxes and solstices. Each plot reports, for the corresponding case study, the weighted average of the **r** profiles retrieved from the four sets of observations indicated in Table 1. The isotope ratio profiles in Figure 5 show that at altitudes roughly ranging between 15 and 25 km, the atmosphere is generally enriched in the heavier HNO_3 isotopologue with respect to the natural isotope ratio (**r** = 1). Above 25 km, a decrease of the $H^{15}NO_3$ isotopologue becomes more

Table 1. MIPAS Data Used for the Retrieval of **r**[a]

Code	Part of Figure 5	Sets of MIPAS Measurements
EQU-e	Figure 5a	20–24 Sep 2002 (358), 20–24 Sep 2003 (425), 19–23 Mar 2003 (430), 9–13 Mar 2004 (406)
EQU-s	Figure 5b	19–26 Dec 2002 (430), 19–26 Dec 2003 (430), 17–24 Jul 2002 (430), 16–24 Jun 2003 (430)
MID-e	Figure 5c	20–22 Sep 2002 (430), 22–23 Sep 2003 (430), 20–22 Mar 2003 (430), 21–22 Mar 2004 (430)
MID-s	Figure 5d	20–22 Dec 2002 (430), 20–22 Dec 2003 (430), 17–18 Jul 2002 (430), 16–18 Jun 2003 (430)
NP-e	Figure 5e	20–24 Sep 2002 (430), 20–24 Sep 2003 (305), 18–27 Mar 2003 (314), 7–18 Mar 2004 (350)
NP-s	Figure 5f	20–24 Dec 2002 (430), 20–25 Dec 2003 (406), 17–21 Jul 2002 (430), 16–21 Jun 2003 (430)
SP-e	Figure 5g	20–24 Sep 2002 (350), 20–24 Sep 2003 (306), 18–27 Mar 2003 (430), 7–18 Mar 2004 (430)
SP-s	Figure 5h	20–25 Dec 2002 (345), 20–30 Dec 2003 (335), 17–21 Jul 2002 (430), 16–23 Jun 2003 (398)

[a]First column gives the latitude band and equinox (-e) or solstice (-s) condition of the mean profile. Second column gives the part of Figure 5 reporting the corresponding weighted mean profile. Third column gives the time interval of measurements and number of scans sequentially processed for the retrieval of each **r** profile.

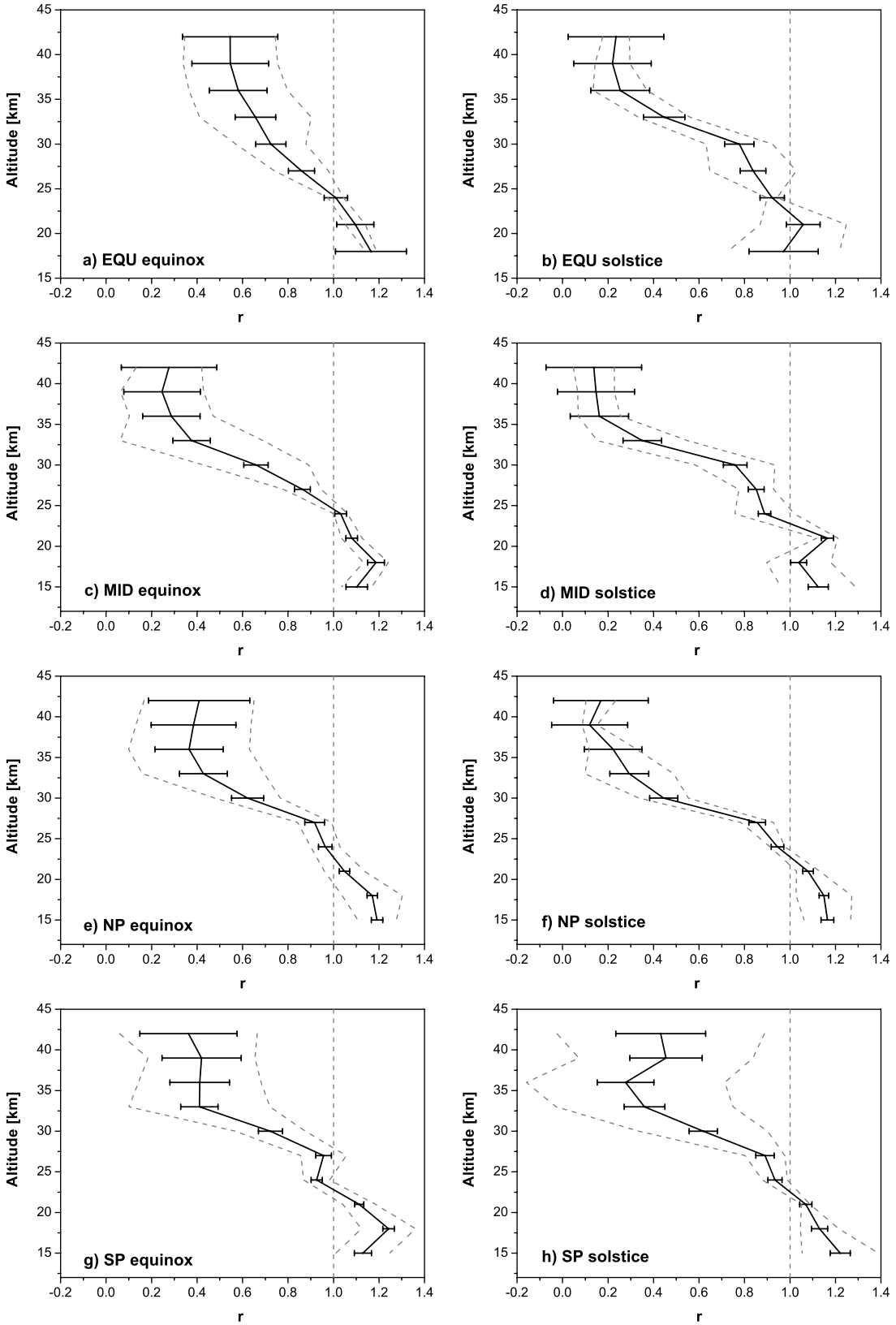

Figure 5. Mean profiles of **r** for equinox and solstice conditions. Latitude bands are as follows: (a and b) equatorial (EQU), (c and d) midlatitudes (MID), (e and f) North Pole (NP), and (g and h) South Pole (SP). Each profile is the weighted mean of four profiles retrieved from the observations indicated in Table 1. Error bars represent the random error of the mean due to measurement noise. The dashed lines indicate the standard deviation of the profiles used to calculate the average. The vertical line represents the initial guess profile **r** = 1.

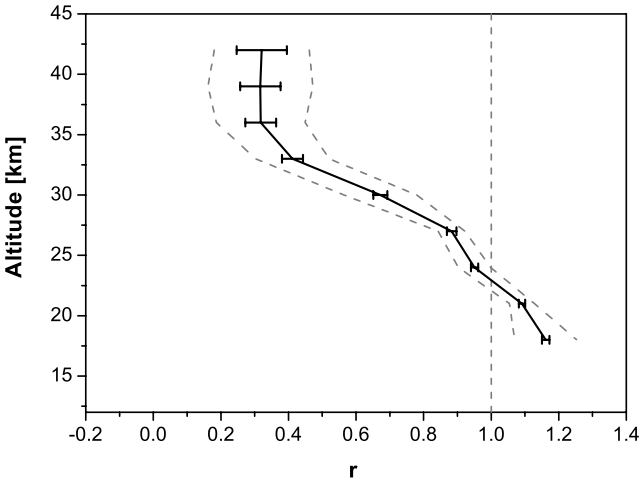

Figure 6. Global average **r** profile obtained from equinox and solstice profiles reported in Figure 5.

marked as altitude increases. The above described features are common to the isotope ratio profiles obtained for all the eight considered case studies. Actually, if the profiles of Figure 5 are plotted on a single graph, the overlapping of the error bars indicates that in stratospheric nitric acid, temporal and latitudinal variations of the $^{15}N/^{14}N$ ratio are of minor entity. It is therefore meaningful to calculate an overall average of the **r** profiles shown in Figure 5. The weighted average of these profiles is shown in Figure 6 and reported in Table 2 also with the δ notation given in equation (2). Because of the presence of high-altitude clouds, most of the MIPAS equatorial measurements extended down to only 18 km, therefore the average profile was limited to this altitude.

[45] The **r** profiles reported in this section are represented on a 3 km altitude grid (that coincides with the retrieval grid) that matches the sampling step of the MIPAS limb measurements. However, the spacing between consecutive points of the altitude grid does not represent the vertical resolution of the profiles that as discussed by *Rodgers* [2000], can be calculated as FWHM of the AKs. The AKs for the **r** profiles relative to the equinoxes in 2003 are given in Figure 7, also with the number of degrees of freedom calculated as the trace of the AK matrix [*Rodgers*, 2000]. It results that 3 to 6 DOFs were generally obtained. The lower values of the DOF at the equator are due to the reduced vertical range at which the retrieval was performed and to the higher number of cloud-contaminated sweeps rejected by the cloud filtering process in the analyzed scans. Examples of the actual vertical resolution of the **r** profiles are provided in Figure 8. The two plots of Figure 8 show the vertical resolution of the **r** profiles for each case of Figure 7. In general, the vertical resolution of the **r** profiles, in the altitude range where the final random error is low, is close to the measurements vertical step.

7. Conclusions

[46] As a next step following the identification of $H^{15}NO_3$ in MIPAS observations, we used MIPAS high-resolution infrared limb emission spectra to measure, for the first time, the $^{15}N/^{14}N$ isotope ratio in stratospheric nitric acid. For this purpose we developed a dedicated inversion procedure based on an iteratively regularized sequential, linear Kalman filter. This retrieval procedure is generally applicable to cases where the target parameter of the inversion has a very poor signal-to-noise ratio and therefore large sets of observations need to be merged to infer a single (average) estimate of the target with reasonable accuracy.

[47] We retrieved $H^{15}NO_3/H^{14}NO_3$ isotope ratio profiles in the range from 18 to 42 km with a number of degrees of freedom ranging from 3 to 6. The best accuracy of about 10% was achieved in the altitude range from 20 to 25 km, where nitric acid is mostly concentrated. The behavior of the isotope ratio was studied for different latitude bands and seasons.

[48] The $^{15}N/^{14}N$ partitioning in stratospheric nitric acid shows a systematic deviation from the natural isotope ratio: between 15 and 25 km the atmosphere is enriched in $H^{15}NO_3$ while, above 25 km, the heavier isotopologue shows a depletion that becomes markedly stronger with altitude. This overall trend is common to the isotope ratio profiles obtained for all the eight considered case studies indicating that in the stratosphere, seasonal and latitudinal variations appear not to affect significantly the $^{15}N/^{14}N$ nitric acid distribution. Because of the compatibility among all profiles, we also provided a global average profile of $H^{15}NO_3/H^{14}NO_3$, i.e., an overall picture of the $^{15}N/^{14}N$ partitioning in stratospheric nitric acid. Our results show that above 25 km, the $^{15}N/^{14}N$ isotopic fractionation in HNO_3 behaves in the opposite direction with respect to N_2O.

[49] A large number of physical and chemical mechanisms, such as the escape rate of heavy and light isotopologues as a function of their mass, and the different rate of chemical reactions involving isotopically substituted species, is known to drive the atmospheric isotopic fractionation [*Johnson et al.*, 2002]. Nevertheless the interpretation of the mechanisms leading to the $^{15}N/^{14}N$ distribution reported is far beyond the possibilities of the present paper. No complemental studies exist on atmospheric ^{15}N nitric acid. These novel measurements provide observational evidence of atmospheric mechanisms not yet explored, and call for laboratory experiments and chemical atmospheric models to be used to bring forward additional knowledge of the underlying chemical and physical processes. Only the integrated use of modeling studies and observations providing valuable information to input into global models could

Table 2. Global Average **r** Profile Obtained From the Equinox and Solstice Profiles Reported in Figure 5[a]

Height (km)	**r**	Noise Error	Standard Deviation	δ (‰)
42	0.321	0.074	0.140	−679
39	0.317	0.060	0.156	−683
36	0.318	0.046	0.131	−682
33	0.412	0.031	0.109	−588
30	0.672	0.021	0.108	−328
27	0.883	0.014	0.040	−117
24	0.951	0.011	0.048	−49
21	1.091	0.010	0.037	91
18	1.161	0.011	0.092	161

[a]Noise error and standard deviation are also indicated relative to **r**. The data in the first four columns are the values plotted in Figure 6.

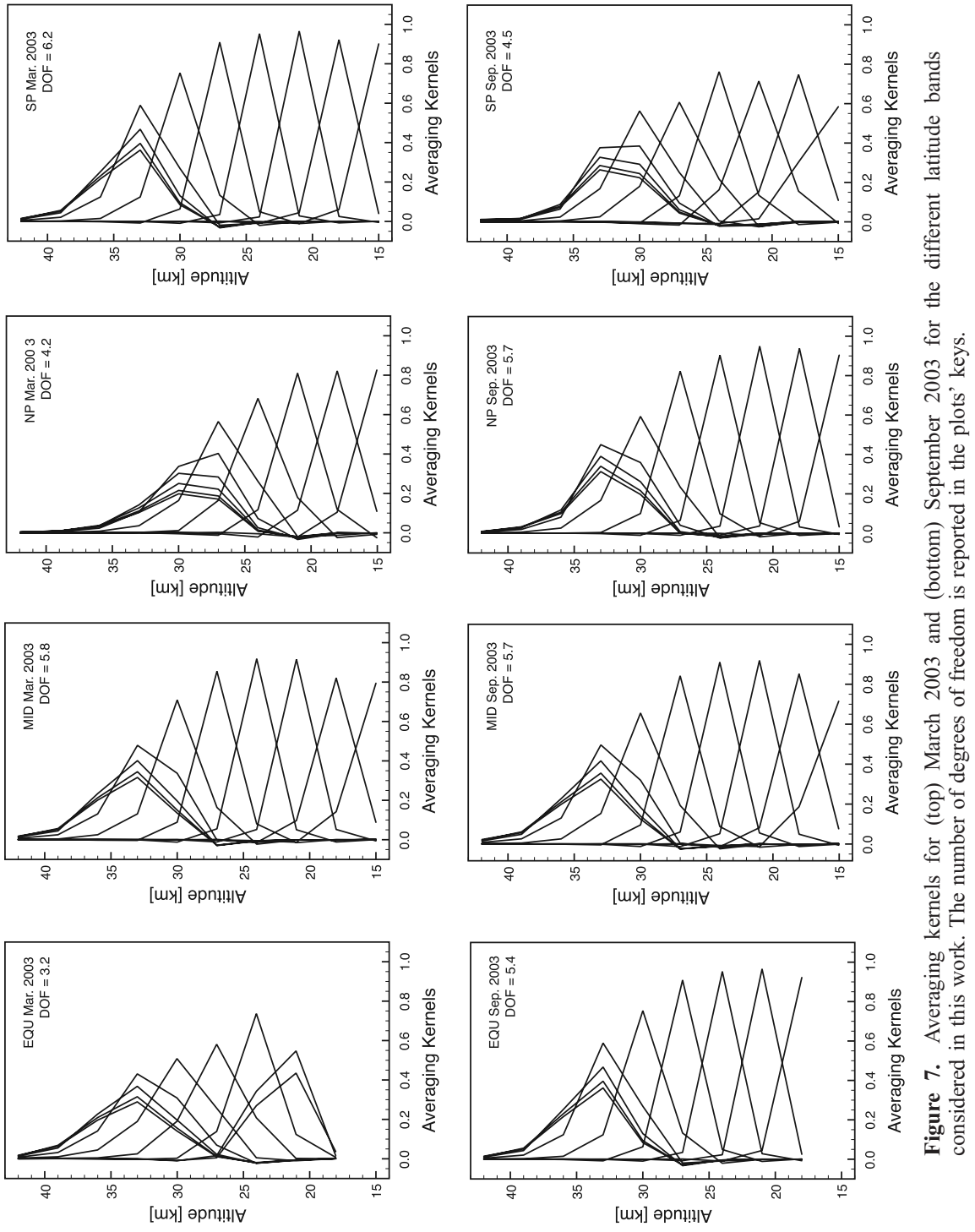

Figure 7. Averaging kernels for (top) March 2003 and (bottom) September 2003 for the different latitude bands considered in this work. The number of degrees of freedom is reported in the plots' keys.

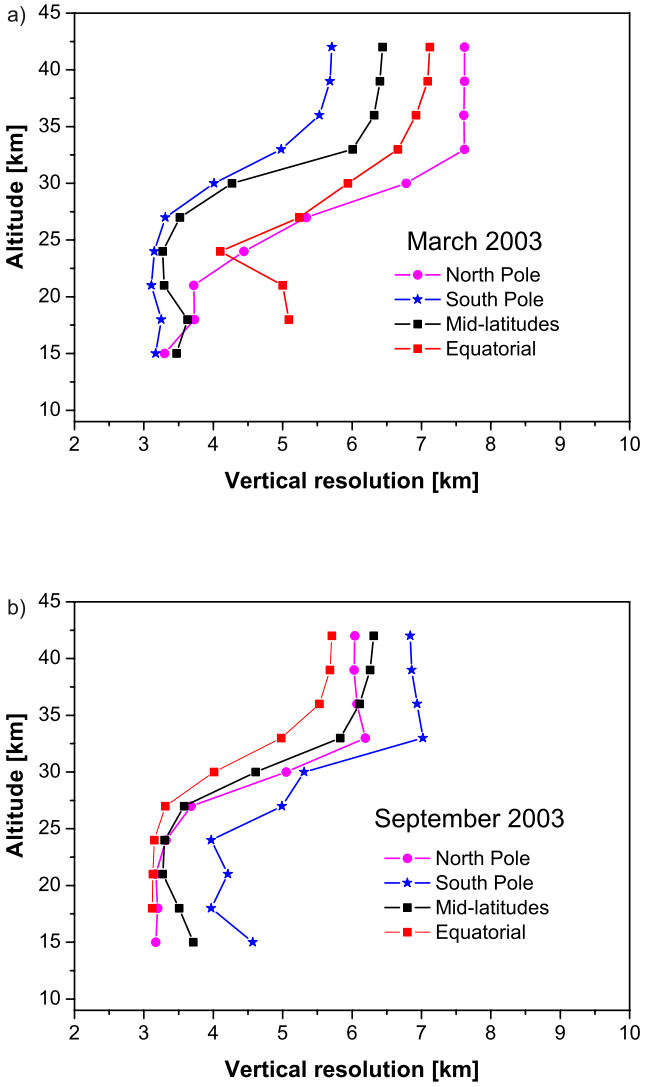

Figure 8. Vertical resolution calculated as the full width at half maximum of the averaging kernels of Figure 7, for (top) March 2003 and (bottom) September 2003, for different latitude bands.

account for the observed nitric acid isotope distribution, possibly identifying and quantifying the active mechanisms.

[50] **Acknowledgments.** The authors are grateful to Simone Ceccherini for fruitful discussions regarding the retrieval approach developed as part of this work. G. Brizzi gratefully acknowledges Kelly Chance for the valuable opportunity of working at CfA and funding through the NASA grant NNG05GO08G. E. Arnone acknowledges funding through the European Community's Human Potential Programme Marie Curie under contract MERG-CT-2007-209157.

References

Arnone, E., and M. Carlotti (2008), Check day/night CFC-11 for the GMTR data, *Tech. Note AI_L1_17.06*, Eur. Space Agency, Paris.

Arnone, E., et al. (2009), Impact of horizontal temperature gradient on CFC-11 fields retrieved from MIPAS limb sounding: One-dimensional approach versus two-dimensional tomography, paper presented at the 14th Workshop on Atmospheric Science from Space using Fourier Transform Spectrometry, Sesto Fiorentino, Italy, May.

Austin, J., R. R. Garcia, J. M. Russell III, S. Solomon, and A. F. Tuck (1986), On the atmospheric photochemistry of nitric acid, *J. Geophys. Res.*, *91*(D5), 5477–5485.

Beer, R., T. A. Glavich, and D. M. Rider (2001), Tropospheric emission spectrometer for the Earth Observing System's Aura satellite, *Appl. Opt.*, *40*, 2356–2367.

Bernath, P. F., et al. (2005), Atmospheric Chemistry Experiment (ACE): Mission overview, *Geophys. Res. Lett.*, *32*, L15S01, doi:10.1029/2005GL022386.

Blom, C. E., H. Fischer, N. Glatthor, T. Gulde, M. Hopfner, and C. Piesch (1995), Spatial and temporal variability of $ClONO_2$, HNO_3 and O_3 in the Arctic winter of 1992/1993 as obtained by airborne infrared emission spectroscopy, *J. Geophys. Res.*, *100*(D5), 9101–9114.

Brizzi, G., M. Carlotti, J.-M. Flaud, A. Perrin, and M. Ridolfi (2007), First observation of $H^{15}NO_3$ in atmospheric spectra, *Geophys. Res. Lett.*, *34*, L03802, doi:10.1029/2006GL028395.

Carli, B., et al. (2004), First results of MIPAS/ENVISAT with operational Level 2 code, *Adv. Space Res.*, *33*, 1012–1019.

Carlotti, M., G. Brizzi, E. Papandrea, M. Prevedelli, M. Ridolfi, B. M. Dinelli, and L. Magnani (2006), GMTR: Two-dimensional multi-target retrieval model for MIPAS-ENVISAT observations, *Appl. Opt.*, *45*(4), 716–727.

Dinelli, B. M., D. Alpaslan, M. Carlotti, L. Magnani, and M. Ridolfi (2004), Multi-target retrieval (MTR): The simultaneous retrieval of pressure, temperature and volume mixing ratio profiles from limb-scanning atmospheric measurements, *J. Quant. Spectrosc. Radiat. Transfer*, *84*, 141–157.

Doicu, A., F. Schreier, and M. Hess (2004), Iterative regularization methods for atmospheric remote sensing, *J. Quant. Spectrosc. Radiat. Transfer*, *83*, 47–61.

Dudhia, A., V. L. Jay, and C. D. Rodgers (2002), Microwindow selection for high-spectral-resolution sounders, *Appl. Opt.*, *41*(18), 3665–3673.

Fischer, H., et al. (1997), Observations of high concentrations of total reactive nitrogen (NO_y) and nitric acid (HNO_3) in the lower Arctic stratosphere during the Stratosphere-Troposphere Experiment by Aircraft Measurements (STREAM) II campaign in February 1995, *J. Geophys. Res.*, *102*(D19), 23,559–23,571.

Fischer, H., et al. (2000), *ENVISAT-MIPAS: An Instrument for Atmospheric Chemistry and Climate Research*, edited by C. Readings and R. A. Harris, *Eur. Space Agency Spec. Publ., ESA SP-1229*.

Fischer, H., et al. (2008), MIPAS: An instrument for atmospheric and climate research, *Atmos. Chem. Phys.*, *8*, 2151–2188.

Flaud, J.-M., A. Perrin, J. Orphal, Q. Kou, P.-M. Flaud, Z. Dutkiewicz, and C. Piccolo (2003a), New analysis of the $\nu_5 + \nu_9 - \nu_9$ hot band of HNO_3, *J. Quant. Spectrosc. Radiat. Transfer*, *77*, 355–364.

Flaud, J.-M., C. Piccolo, B. Carli, A. Perrin, L. H. Coudert, J.-L. Teffo, and L. R. Brown (2003b), Molecular line parameters for the MIPAS (Michelson Interferometer for Passive Atmospheric Sounding) experiment, *Atmos. Oceanic Opt.*, *16*, 172–182.

Flaud, J.-M., G. Brizzi, M. Carlotti, A. Perrin, and M. Ridolfi (2006), MIPAS database: Validation of HNO_3 line parameters using MIPAS satellite measurements, *Atmos. Chem. Phys.*, *6*, 5037–5048.

Griesfeller, A., J. Griesfeller, F. Hase, I. Kramer, P. Loes, S. Mikuteit, U. Raffalski, T. Blumenstock, and H. Nakajima (2006), Comparison of ILAS-II and ground-based FTIR measurements of O_3, HNO_3, N_2O, and CH_4 over Kiruna, Sweden, *J. Geophys. Res.*, *111*, D11S07, doi:10.1029/2005JD006451.

Griffith, D., G. Toon, B. Sen, J. Blavier, and R. Toth (2000), Vertical profiles of nitrous oxide isotopomer fractionation measured in the stratosphere, *Geophys. Res. Lett.*, *27*(16), 2485–2488.

Gunson, M. R., et al. (1996), The Atmospheric Trace Molecule Spectroscopy (ATMOS) experiment: Deployment on the ATLAS Space Shuttle missions, *Geophys. Res. Lett.*, *23*, 2333–2336.

Hartogh, P., and P. J. Espy (Eds.) (2006–2009), MIPAS (Michelson Interferometer for Passive Atmosphere Sounding): Potential of the experiment, data processing and validation of results, *Atmos. Chem. Phys.*, 6–9.

Johnson, M. S., K. L. Feilberg, P. von Hessberg, and O. J. Nielsen (2002), Isotopic processes in atmospheric chemistry, *Chem. Soc. Rev.*, *31*, 313–323.

Kaiser, J., C. A. M. Brenninkmeijer, and T. Röckmann (2002), Intramolecular ^{15}N and ^{18}O fractionation in the reaction of N_2O with $O(^1D)$ and its implications for the stratospheric N_2O isotope signature, *J. Geophys. Res.*, *107*(D14), 4214, doi:10.1029/2001JD001506.

Kaiser, J., A. Engel, R. Borchers, and T. Röckmann (2006), Probing stratospheric transport and chemistry with new balloon and aircraft observations of the meridional and vertical N_2O isotope distribution, *Atmos. Chem. Phys. Discuss.*, *6*, 4273–4324.

Kalman, R. E. (1960), A new approach to linear filtering and prediction problems, *J. Basic Eng.*, *82*(1), 35–45.

Kaye, J. A. (1987), Mechanisms and observations for isotope fractionation of molecular species in planetary atmospheres, *Rev. Geophys.*, *25*(8), 1609–1658.

Koike, M., et al. (2000), A comparison of Arctic HNO_3 profiles measured by the Improved Limb Atmospheric Spectrometer and balloon-borne sensors, *J. Geophys. Res.*, *105*(D5), 6761–6771.

Lide, D. R., (Ed.) (2000), *CRC Handbook of Chemistry and Physics*, 80th ed., CRC Press, Boca Raton, Fla.

Meier, A., C. Paton-Walsh, W. Bell, T. Blumenstock, F. Hase, A. Goldman, A. Steen, R. Kift, P. Woods, and K. Kondo (2005), Evidence of reduced measurement uncertainties from an FTIR instrument intercomparison at Kiruna, Sweden, *J. Quant. Spectrosc. Radiat. Transfer*, *96*, 75–84.

Mencaraglia, F., G. Bianchini, A. Boscaleri, B. Carli, S. Ceccherini, P. Raspollini, A. Perrin, and J.-M. Flaud (2006), Validation of MIPAS satellite measurements of HNO_3 using comparison of rotational and vibrational spectroscopy, *J. Geophys. Res.*, *111*, D19305, doi:10.1029/2005JD006099.

Oelhaf, H., T. von Clarmann, H. Fischer, F. Friedl-Vallon, C. Frizsche, A. Linden, C. Piesch, M. Seefeldner, and W. Volker (1994), Stratospheric $ClONO_2$ and HNO_3 profiles inside the Arctic Vortex from MIPAS-B limb emission spectra obtained during EASOE, *Geophys. Res. Lett.*, *21*, 1263–1266.

Park, S., E. L. Atlas, and K. A. Boering (2004), Measurements of N_2O isotopologues in the stratosphere: Influence of transport on the apparent enrichment factors and the isotopologue fluxes to the troposphere, *J. Geophys. Res.*, *109*, D01305, doi:10.1029/2003JD003731.

Payne, V., A. Dudhia, and C. Piccolo (2004), Isotopic measurements of water vapour and methane from the MIPAS satellite instrument, *Eos Trans. AGU*, *85*(47), Fall Meet. Suppl., Abstract A21B-0733.

Payne, V. H., D. Noone, A. Dudhia, C. Piccolo, and R. G. Grainger (2007), Global satellite measurements of HDO and implications for understanding the transport of water vapour into the stratosphere, *Q. J. R. Meteorol. Soc.*, *133*, 1459–1471.

Perrin, A., and R. Mbiaké (2006), The ν_5 and $2\nu_9$ bands of the ^{15}N isotopic species of nitric acid ($H^{15}NO_3$): Line positions and intensities, *J. Mol. Spectrosc.*, *237*, 27–35.

Piccolo, C., A. Dudhia, and V. Payne (2007), Global observations of ozone isotopic ratios from MIPAS limb emission spectra, in *Proceedings of the Envisat Symposium 2007, Montreux, Switzerland, July 2007* [DVD], edited by H. Lacoste and L. Ouwehand, Eur. Space Agency Spec. Publ., *ESA SP-636*.

Raspollini, P., et al. (2006), MIPAS level 2 operational analysis, *Atmos. Chem. Phys.*, *6*, 5605–5630.

Remedios, J. J., R. J. Leigh, A. M. Waterfall, D. P. Moore, H. Sembhi, I. Parkes, J. Greenhough, M. P. Chipperfield, and D. Hauglustaine (2007), MIPAS Reference Atmospheres and comparisons to v4.61/v4.62 MIPAS level 2 geophysical data sets, *Atmos. Chem. Phys. Discuss.*, *7*, 9973–10017.

Ridolfi, M., et al. (2000), Optimized forward model and retrieval scheme for MIPAS near-real-time data processing, *Appl. Opt.*, *39*(8), 1323–1340.

Rinsland, C. P., R. Zander, and P. Demoulin (1991), Ground-based infrared measurements of HNO_3 total column abundances: Long term trend and variability, *J. Geophys. Res.*, *96*(D5), 9379–9389.

Rodgers, C. D. (2000), *Inverse Methods for Atmospheric Sounding: Theory and Practice*, *Ser. on Atmos., Oceanic and Planet. Phys.*, vol. 2, pp. 65–100, World Sci., Singapore.

Russell, J. M., C. B. Farmer, C. P. Rinsland, R. Zander, L. Froidevaux, G. C. Toon, B. Gao, J. Shaw, and M. Gunson (1988), Measurements of odd nitrogen compounds in the stratosphere by the ATMOS experiment on Spacelab3, *J. Geophys. Res.*, *93*(D2), 1718–1736.

Spang, R., J. Remedios, and M. Barkley (2004), Cloud indices for the detection and differentiation of cloud types in infrared limb emission spectra, *Adv. Space Res.*, *33*, 1041–1047.

Steinwagner, J., M. Milz, T. von Clarmann, N. Glatthor, U. Grabowski, M. Hopfner, G. P. Stiller, and T. Rockmann (2007), HDO measurements with MIPAS, *Atmos. Chem. Phys.*, *7*, 2601–2615.

Toon, G. C., C. B. Farmer, L. L. Lowes, P. W. Schaper, J. F. Blavier, and R. H. Norton (1989), Infrared aircraft measurements of stratospheric composition over Antarctica during September 1987, *J. Geophys. Res.*, *94*(D14), 16,571–16,596.

Toyoda, S., et al. (2004), Temporal and latitudinal distributions of stratospheric N_2O isotopomers, *J. Geophys. Res.*, *109*, D08308, doi:10.1029/2003JD004316.

von Clarmann, T., H. Fischer, F. Friedl-Vallon, A. Linden, H. Oelhaf, C. Piesch, and M. Seefeldner (1993), Retrieval of stratospheric O_3, HNO_3, and $ClONO_2$ profiles from 1992 MIPAS-B Limb emission spectra: Method, results and error analysis, *J. Geophys. Res.*, *98*(D11), 20,495–20,506.

Wang, D. Y., et al. (2007), Validation of MIPAS HNO_3 operational data, *Atmos. Chem. Phys.*, *7*, 4905–4934.

World Meteorological Organization (2003), Scientific assessment of ozone depletion: 2002, *Global Ozone Res. and Monit. Proj., Rep. 47*, Geneva, Switzerland.

E. Arnone, M. Carlotti, E. Papandrea, and M. Ridolfi, Dipartimento di Chimica Fisica e Inorganica, Università di Bologna, Viale del Risorgimento, 4, I-40136 Bologna, Italy. (arnone@fci.unibo.it; carlotti@fci.unibo.it; enzo@safire.fci.unibo.it; ridolfi@fci.unibo.it)

G. Brizzi, Harvard-Smithsonian Center for Astrophysics, 60 Garden Street, MS-50, Cambridge, MA 02138, USA. (gbrizzi@cfa.harvard.edu)

B. M. Dinelli, Istituto di Scienze dell'Atmosfera e del Clima, Consiglio Nazionale delle Ricerche, Via Gobetti, 101, I-40129 Bologna, Italy. (bm.dinelli@isac.cnr.it)

J.-M. Flaud and A. Perrin, Laboratoire Interuniversitaire des Systèmes Atmosphériques, Université Paris 7, Université Paris 12, CNRS, 61 avenue du Général de Gaulle, F-94010 Créteil CEDEX, France. (flaud@lisa.univ-paris12.fr; agnes.perrin@lisa.univ-paris12.fr)